Malaysian Journal of Catalysis
http://mjcat.utm.my/
MJCat
Research Article

Tin-Doped Titanium Dioxide Photocatalysts Prepared via Hydrothermal Method: Effect of Calcination Temperature on Dye Degradation Efficiency

Li Fang See[1], Chui Min Ling[1], Alice Sim Hui Li[1], Ching Shien Lee[1], Siew Ling Lee[1,2*]

[1] *Department of Chemistry, Faculty of Science, Universiti Teknologi Malaysia, 81310 UTM Johor Bahru, Johor, Malaysia*
[2] *Centre for Sustainable Materials, Ibnu Sina Institute for Scientific and Industrial Research, Universiti Teknologi Malaysia, 81310 Johor Bahru, Johor, Malaysia.*

**Corresponding Author: Tel: +60177165916 (lsling@utm.my)*

Article history :
Received 27 March 2026
Revised 16 June 2026
Accepted 22 June 2026

ABSTRACT

The widespread discharge of persistent and toxic synthetic dyes from the textile industry into aquatic ecosystems has critically compromised global access to clean water. Conventional treatment techniques are often inefficient in removing these pollutants. Among advanced oxidation processes, photocatalysis has emerged as a promising solution for degrading dye-contaminated wastewater. While titanium dioxide (TiO_2) is a prominent photocatalyst for wastewater treatment, its practical application is limited by a wide band gap (3.2 eV) and rapid electron-hole recombination. This study reports the preparation of tin-doped titanium dioxide (Sn-doped TiO_2) as a photocatalyst via a hydrothermal method, with a systematic focus on optimizing calcination temperature. The as-prepared photocatalysts were characterized by X-ray diffraction (XRD), which confirmed a pure anatase phase with the crystallite size increased at higher calcination temperature. Scanning electron microscopy (SEM) coupled with energy-dispersive X-ray (EDX) analysis verified the presence of tin within particle clusters, while diffuse reflectance ultraviolet-visible (DR UV-Vis) and Fourier transform infrared (FTIR) spectroscopies confirmed extended visible-light absorption and successful lattice incorporation. Furthermore, photoluminescence (PL) results indicated that Sn-TiO_2 (400 °C) exhibited a more ordered crystal structure, reducing non-radiative recombination. Photocatalytic evaluation via methylene blue (MB) degradation under visible light revealed that Sn-doped TiO_2 calcined at 400 °C achieved the highest efficiency of 65.2% after 7 hours. This enhanced performance was attributed to the synergistic effects of a narrowed band gap (3.14 eV), high crystallinity, and optimized crystallite size. These findings demonstrate that controlling calcination temperature is crucial for developing efficient, visible-light-active photocatalysts for sustainable industrial wastewater remediation.

Keywords: Photocatalysis, Sn-doped TiO_2, Dye Degradation, Calcination Temperature, Hydrothermal

http://dx.doi.org/xx.xxx/xxx.xxx.xxx |

1. INTRODUCTION

Over the past few years, access to clean water has emerged as a critical global concern due to rapid industrial and technological advancements. The textile industry alone produces approximately 7 x 10^5 tons of dyes each year, with up to 10% discharged as wastewater after dyeing and processing [1,2]. Methylene blue (MB) is a synthetic, cationic dye with a heterocyclic aromatic structure. It is frequently used as a model contaminant due to its chemical stability and resistance to degradation [3]. These synthetic dyes, which are primarily derived from coal tar and petroleum intermediates, are toxic, mutagenic, and carcinogenic, posing severe risks to aquatic ecosystems and public health [4,5].

Conventional treatments of dye removal, such as adsorption, coagulation, ion exchange, and biological methods, are widely utilized. While these methods are effective, they are often non-destructive and suffer from major drawbacks, including low decomposition efficiency and secondary waste generation [5,6]. Consequently, heterogeneous photocatalysis, an advanced oxidation process, has emerged as a sustainable alternative capable of mineralizing organic pollutants into harmless by-products such as carbon dioxide and water. This field of research was significantly influenced by the pioneering work of Fujishima and Honda in 1972, who first demonstrated the photolysis of water using a titanium dioxide (TiO_2) photoanode under ultraviolet (UV) irradiation [7]. Since this breakthrough, photocatalysis has gained considerable attention for environmental remediation. This process utilizes light energy to generate short-lived reactive species, specifically hydroxyl radicals (•OH) and superoxide anions ($O_2^{\bullet-}$), to drive the degradation [5,8-10].

TiO_2 is one of the most extensively researched photocatalysts, known for its high stability, cost-effectiveness, non-toxicity, and outstanding optical properties [8,11]. Among its polymorphs, anatase is generally regarded as having higher photocatalytic efficiency than rutile or brookite. This superior performance is driven by its indirect band gap, which extends the lifetimes of photogenerated charge carriers and thereby lowers their recombination rate [11-13]. These properties have enabled it to be utilized in various applications, including solar cells, water and air purification, medical delivery systems, and self-cleaning antibacterial surfaces [14,15].

Despite these advantages, TiO_2 still has its shortcomings. Its wide band gap (3.2 eV) restricts photocatalytic activity to the UV region, which constitutes only about 5% of the solar spectrum, while also suffering from rapid electron-hole (e^-/h^+) recombination [2,16]. Metal doping serves as an effective strategy to narrow the band gap, extend light absorption into the visible range, and suppress e^-/h^+ recombination [2,8]. Among various dopants, tin is more effective compared to alternatives like noble metals and transition metals. This effectiveness stems from the comparable ionic radii of Sn^{4+} (0.690 Å) and Ti^{4+} (0.605 Å), which favors its incorporation into the TiO_2 lattice [17,18]. This structural compatibility facilitates easier lattice substitution and suppresses the undesirable phase transformation from anatase to rutile [2,17,18]. Furthermore, the incorporated Sn^{4+} ions alter the electronic structure by introducing new states within the band gap, narrowing the gap and inducing a red shift that significantly enhances visible-light absorption. Concurrently, these dopant sites act as localized electron traps that capture photogenerated electron-hole pairs, thereby suppressing recombination [19-21]. This mechanism aligns with recent findings on Sn-doped TiO_2 nanostructures, which demonstrate that optimizing the Sn dopant concentration exerts a profound synergic effect on visible-light utilization by modifying the electronic properties and inhibiting electron-hole recombination [22,23].

Sn-doped TiO_2 photocatalysts have been synthesized via various techniques, including sol-gel, hydrothermal, and chemical vapor deposition [17,24]. Among these, the hydrothermal method is particularly advantageous for yielding highly crystalline products with a narrow particle size distribution and excellent dispersion, achieved by controlling crystal growth under elevated vapor pressures [16,24,25]. Despite the potential of Sn-doped TiO_2, the physicochemical properties of the resulting catalysts remain strongly dependent on the calcination temperature, which serves as a critical parameter governing phase transformation, crystallite size, and crystallinity [26]. While moderate calcination can enhance crystallinity and charge mobility, excessively elevated temperatures may cause over-sintering and promote grain growth, thereby reducing available active sites and the specific surface area (SSA), subsequently diminishing overall photocatalytic activity [17, 27].

While considerable research has been dedicated to optimizing dopant concentrations within Sn-doped TiO_2 [28,29], the precise role of post-synthesis thermal treatment in regulating the properties and subsequent visible-light performance remains a critical, underexplored variable. This study addresses this gap by preparing Sn-doped TiO_2 photocatalysts via a hydrothermal method with a fixed Sn content, systematically isolating the effects of calcination temperature on physicochemical properties and subsequent photocatalytic behavior. The structural, morphological, and optical characteristics of the prepared materials were comprehensively investigated. Subsequently, their photocatalytic efficiency was assessed by photodegrading MB under visible light. By demonstrating effective photocatalytic degradation of MB, this study provides a promising development toward an efficient photocatalyst for industrial wastewater remediation.

2. EXPERIMENTS

2.1 Preparation of Sn-doped TiO_2 photocatalysts

Sn-doped TiO_2 photocatalysts were prepared using a hydrothermal method adapted from previously reported procedures [30]. Initially, 2.5 g of commercial anatase TiO_2 was dispersed in 50 mL of absolute ethanol and stirred vigorously for one hour. To this dispersion, $SnCl_4 \cdot 5H_2O$ was added to achieve a 5 mol% Sn doping level relative to Ti. The mixture was stirred for 2 hours at ambient temperature, after which the pH was adjusted to 7 by the gradual addition of ammonia solution. The resulting suspension was transferred to a 50 mL Teflon-lined stainless-steel autoclave and subjected to hydrothermal treatment at 180 °C for 24 hours. Following the reaction, the autoclave was cooled naturally to room temperature. The obtained precipitates were subjected to repeated washing with deionized water and ethanol via centrifugation, then dried at 80 °C overnight. Finally, the dried samples were calcined at 300 °C for 2 hours with a heating rate of 5 °C/min. The procedure was repeated to prepare other photocatalysts, denoted as Sn-TiO_2 x °C (x = 400, 500, 600 and 700).

2.2 Characterization

The physicochemical properties of the prepared Sn-doped TiO_2 photocatalysts were characterized using several instrumental techniques. The crystallinity and phase purity of the prepared photocatalysts were determined using powder X-ray diffraction (XRD) with a Rigaku MiniFlex II diffractometer. The microscopic surface morphology and elemental composition were investigated using scanning electron microscopy (SEM) coupled with energy-dispersive X-ray (EDX) analysis on a Hitachi TM3000 tabletop microscope equipped with the SwiftED3000 system. The optical properties and band gap energies were examined using diffuse reflectance ultraviolet-visible (DR UV-Vis) spectroscopy on a Shimadzu UV-3600 Plus UV-Vis-NIR spectrophotometer. The functional groups present in the

photocatalysts were identified using Fourier transform infrared (FTIR) spectroscopy on a PerkinElmer Frontier spectrometer using the KBr method. Finally, the charge-carrier recombination rate was evaluated using photoluminescence (PL) spectroscopy to investigate the electronic transition behaviour of the doped materials.

2.3 Photocatalytic degradation of MB

The photocatalytic performance of the prepared photocatalysts was assessed based on the photodegradation of MB under visible light irradiation. Prior to photocatalytic testing, adsorption tests were conducted in the dark to quantify the dye uptake of each photocatalyst. The adsorption ability of each catalyst was tested by withdrawing aliquots at 30-minute intervals until equilibrium was reached. These tests ensured that the observed decrease in dye concentration during irradiation was primarily due to photocatalytic degradation rather than surface adsorption.

In each trial, 0.1 g of the photocatalyst was dispersed in 50 mL of a 10 ppm MB solution and stirred in the dark for 1 hour to establish adsorption-desorption equilibrium. Subsequently, the suspension was irradiated with a 15W Megaman LED bulb serving as the visible light source, positioned 10 cm from the solution, with the experimental setup depicted in **Figure 1**.

Aliquots were sampled at 1-hour intervals for 7 hours and filtered using a membrane syringe filter to separate the photocatalyst. The residual MB concentration was monitored at λ_{max} = 664 nm using a Shimadzu UV-1800 UV-Vis spectrophotometer. The percentage of photodegradation was calculated using Equation (1):

$$\text{Photodegradation percentage (\%)} = \frac{C_0 - C_t}{C_0} \times 100\% \quad (1)$$

where C_0 and C_t are the initial and final concentrations of MB (ppm), respectively.

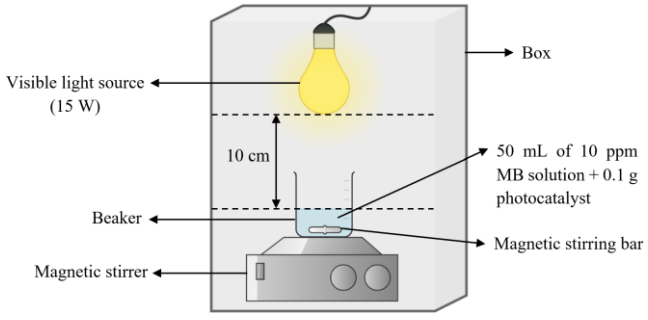

Figure 1. Experimental set up for photodegradation of MB

3. RESULTS AND DISCUSSION

3.1 Characterization of photocatalysts

The XRD diffraction patterns for (a) pure anatase TiO_2, (b) Sn-TiO_2 (400 °C), and (c) Sn-TiO_2 (700 °C) are illustrated in **Figure 2**. The diffraction patterns showed that pure TiO_2 exhibited an anatase phase with distinct peaks at 2θ = 25.25°, 37.72°, 47.97°, 53.79°, 54.97°, 62.63°, 68.71°, 70.17°, and 74.98°, corresponding to the (101), (004), (200), (105), (211), (204), (116), (220), and (215) lattice planes, respectively. These diffraction peaks matched the standard ICDD PDF card no. 5000223. The XRD patterns revealed no peaks corresponding to rutile or brookite phases, indicating that Sn incorporation successfully maintained the anatase lattice without inducing phase transformation [11]. Doping of 5 mol% Sn did not alter the anatase structure, and no additional peaks from Sn species were observed. This suggests that Sn was successfully incorporated into the TiO_2 lattice or highly dispersed on the surface without forming separate phases. Notably, as the calcination temperature increased from 400 °C to 700 °C, the intensity of the characteristic anatase peaks slightly decreased, implying that the anatase phase became thermally unstable at 700 °C.

The average crystallite size of the prepared materials was estimated using the Scherrer equation, with the corresponding values summarized in **Table 1**. Upon introducing the dopant, the crystallite size of pure TiO_2 (72.48 nm) decreased to 66.78 nm. This reduction is attributed to lattice distortion caused by the substitution of larger Sn^{4+} ions into the TiO_2 lattice. At 700 °C, the size increased to 70.66 nm, a trend consistent with grain growth during thermal treatment [31,32]. The relatively large crystallite size observed at this elevated temperature is a direct consequence of thermal treatment. As established in the literature, this higher temperature promotes the crystallization of TiO_2 grains, thereby increasing the grain diameter [33] and triggering further thermal grain growth [34].

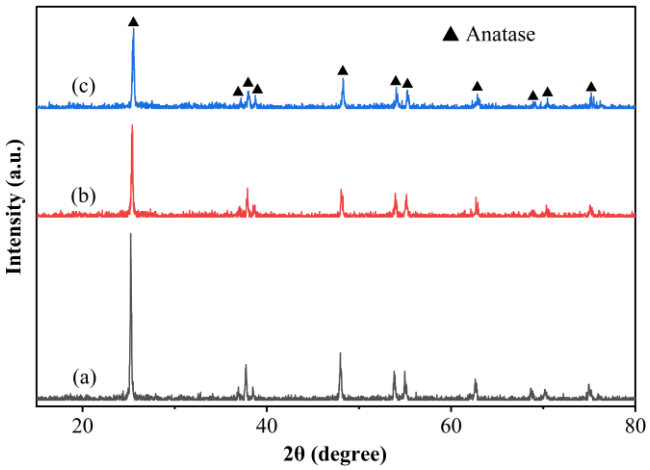

Figure 2. XRD patterns of (a) pure anatase TiO_2, (b) Sn-TiO_2 (400 °C), and (c) Sn-TiO_2 (700 °C)

Table 1. Average crystallite size of pure TiO_2 and Sn-TiO_2 photocatalysts

Sample	Average crystallite size (nm)
Pure TiO_2	72.48
Sn-TiO_2 (400 °C)	66.78

Sn-TiO_2 (700 °C)	70.66

The morphology of the pure anatase TiO_2 is presented in **Figure 3**. For comparison, the morphology of the optimized Sn-TiO_2 (400 °C) photocatalyst is depicted in **Figure 4**. Both samples exhibited similar morphological characteristics, consisting of irregular clusters formed by particles of varying sizes. The EDX elemental analysis of the samples is summarized in **Table 2**. The analysis revealed high weight percentage for titanium (Ti) and oxygen (O), confirming the high purity of the TiO_2 framework. Furthermore, a low Sn weight percentage was observed in the doped sample, confirming successful metal incorporation despite its low weight percentage. However, the recorded weight percentage of Sn in the Sn-TiO_2 (400 °C) sample (0.80 wt%) deviated from the theoretical loading (7.26 wt%). A plausible explanation for this discrepancy is that a portion of the Sn precursor remained unreacted or underwent leaching by ethanol and deionized water during the hydrothermal and washing processes prior to thermal fixation by calcination.

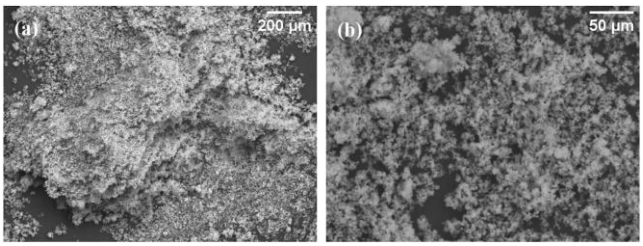

Figure 3. SEM images of pure TiO_2 with different magnifications (a) 1000x and (b) 5000x

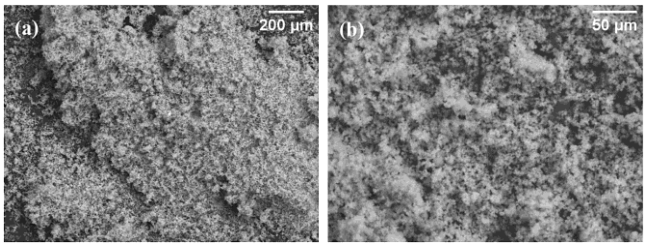

Figure 4. SEM images of Sn-TiO_2 (400 °C) with different magnifications (a) 1000x and (b) 5000x

Table 2. EDX elemental analysis of pure TiO_2 and Sn-TiO_2 (400 °C)

Sample	Weight percentage (%)		
	Ti	O	Sn
Pure TiO_2	55.58	44.42	0.00
Sn-TiO_2 (400 °C)	55.93	43.27	0.80

As illustrated in **Figure 5**, pure anatase TiO_2 and the Sn-doped TiO_2 photocatalysts exhibited a strong, broad absorption band in the UV region (200 – 400 nm). A shoulder observed at approximately 210 nm was attributed to isolated, tetrahedrally coordinated Ti species, arising from charge-transfer transitions between O^{2-} and the central Ti^{4+} ions [35]. Furthermore, the absorption peak at 310 nm corresponds to the electronic transition from the valence band (VB), primarily composed of O_{2p} states, to the conduction band (CB), dominated by Ti_{3d} states of TiO_2 [36,37]. The absorption peak at 330 nm was assigned to polytitanate $(Ti–O–Ti)_n$ or TiO_2 crystals [38].

Compared to TiO_2, the Sn-doped samples displayed a slight red shift in the absorption edge toward the visible light region. This shift is attributed to charge-transfer transitions between the doped Sn^{4+} energy levels and the CB of TiO_2 [39]. These results demonstrate that Sn doping effectively extended the optical absorption range into the visible region, thereby enhancing light absorption of the photocatalysts [2]. Sn-TiO_2 (400 °C) exhibited the most pronounced red shift and the highest visible-light absorbance. This enhancement is attributed to the introduction of new impurity levels within the forbidden band gap of TiO_2 and the formation of surface oxygen vacancies [31,40]. These intermediate states narrow the band gap, thereby generating e^-/h^+ pairs, promoting efficient charge separation and enhancing the overall redox properties [41]. In contrast, pure TiO_2 exhibited the lowest absorbance due to its wide band gap of 3.24 eV. This result matches the standard literature value of 3.2 eV and limits optical absorption to the UV region.

The indirect band gap energy (E_g) of the materials was estimated via Tauc plots, with results summarized in **Table 3**. The incorporation of Sn successfully reduced the E_g of commercial TiO_2 from 3.24 eV to a minimum of 3.14 eV for the sample calcined at 400 °C. This reduction confirmed a bathochromic shift, attributed to the introduction of new Sn^{4+} impurity energy levels within the forbidden band gap, likely to be located just below the CB [31]. These mid-gap states facilitate electronic transitions from the VB using lower excitation energy, thereby promoting efficient charge carrier generation and increasing visible-light utilization [31,42,43]. Furthermore, the doping process likely increased the density of surface oxygen vacancies, which serve as defect states that act as charge-transfer centers, thereby enhancing photocatalytic performance [44,45].

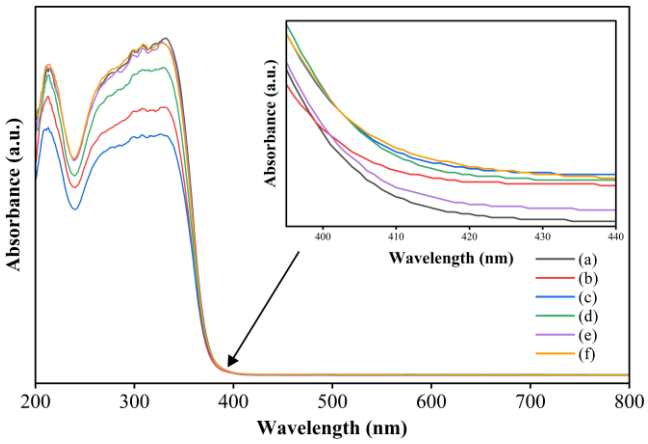

Figure 5. DR UV-Vis spectra of (a) pure TiO_2, (b) Sn-TiO_2 (300 °C), (c) Sn-TiO_2 (400 °C), (d) Sn-TiO_2 (500 °C), (e) Sn-TiO_2 (600 °C), and (f) Sn-TiO_2 (700 °C)

Table 3. Band gap energy of pure TiO_2 and Sn-doped TiO_2 photocatalysts

Sample	Band gap energy, E_g (eV)
Pure TiO_2	3.24
Sn-TiO_2 (300 °C)	3.17
Sn-TiO_2 (400 °C)	3.14
Sn-TiO_2 (500 °C)	3.16
Sn-TiO_2 (600 °C)	3.19
Sn-TiO_2 (700 °C)	3.16

The FTIR spectra of TiO_2 and Sn-TiO_2 (400 °C) in the 4000 – 400 cm^{-1} range are presented in **Figure 6**. Both pure TiO_2 and Sn-TiO_2 (400 °C) exhibited absorption bands at 3430 cm^{-1} and 1633 cm^{-1}, corresponding to the O–H stretching and bending vibrations of surface hydroxyl groups or adsorbed water, respectively [2]. Notably, the Sn-doped sample displayed a higher O–H band intensity, suggesting a greater abundance of surface hydroxyl groups, which may enhance the interaction between the photocatalyst surface and pollutant molecules, thereby facilitating photocatalytic reactions. [44]. These surface hydroxyl groups are critical for the photocatalytic mechanism, as they trap photogenerated h^+ to produce highly reactive hydroxyl radical (•OH) [46]. The band observed at 1384 cm^{-1} was ascribed to the Ti–O–Ti lattice vibration in TiO_2 [47,48]. A distinct broad band observed between 800 – 400 cm^{-1} was assigned to the characteristic vibration modes of Ti–O and Ti–O–Ti bonds. Upon Sn doping, this band widened, indicating the successful formation of Sn–O and Ti–O–Sn bonds within the lattice [49,50]. Specifically, the peak at 696 cm^{-1} corresponded to the Ti vibration of the anatase phase, corroborating the XRD results [51]. Furthermore, the absorption peak at 585 cm^{-1} in the doped sample was attributed to the Sn–O–Sn bond, confirming the successful integration of Sn into the TiO_2 framework [44]. The presence of an intense peak at 1123 cm^{-1} in the Sn-doped TiO_2 sample suggests trace ethanol residues from the washing process, which could be attributed to the C–O stretching vibration.

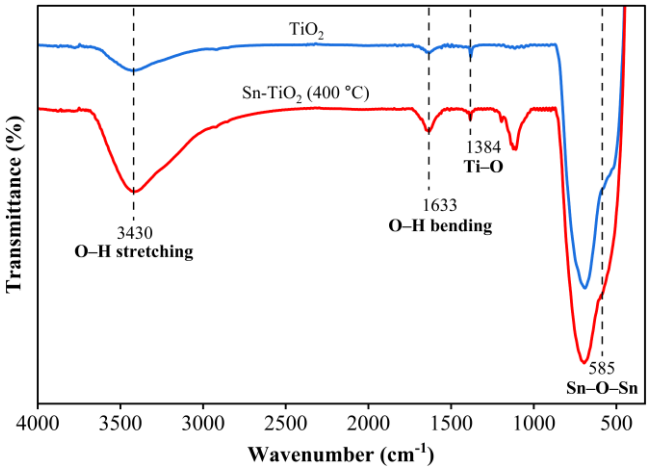

Figure 6. FTIR spectra of pure TiO_2 and Sn-TiO_2 (400 °C)

Figure 7 illustrates the PL emission spectra for pure TiO_2 and the Sn-doped photocatalysts under an excitation wavelength of 320 nm. All samples displayed emission peaks at 395 nm and 418 nm, corresponding to direct recombination of photogenerated e^- in the CB with h^+ in the VB and indirect recombination, respectively [11,52]. Additionally, lower-energy peaks observed between 440 and 480 nm were ascribed to electrons trapped within oxygen vacancies or F-centres [11,31]. These vacancies likely arise from the isomorphic substitution of Ti^{4+} by Sn^{4+}, facilitated by their comparable ionic radii [52].

While a lower PL intensity typically signifies suppressed recombination, the Sn-TiO_2 (400 °C) sample exhibited the highest emission intensity. This phenomenon was attributed to enhanced crystallinity and larger grain size, which effectively suppress non-radiative relaxation pathways. The resulting ordered crystal structure minimized electron scattering and facilitated rapid charge transport to surface-active sites [53]. This ensures that a higher concentration of e^- and h^+ ions can participate in the reaction, thereby enhancing photocatalytic activity. In contrast, the lowest PL intensity was observed for Sn-TiO_2 (700 °C), suggesting a suppressed recombination rate and prolonged charge carrier lifetimes. These results confirmed that Sn doping and optimized calcination temperatures effectively modulate the charge carrier dynamics to enhance photocatalytic activity.

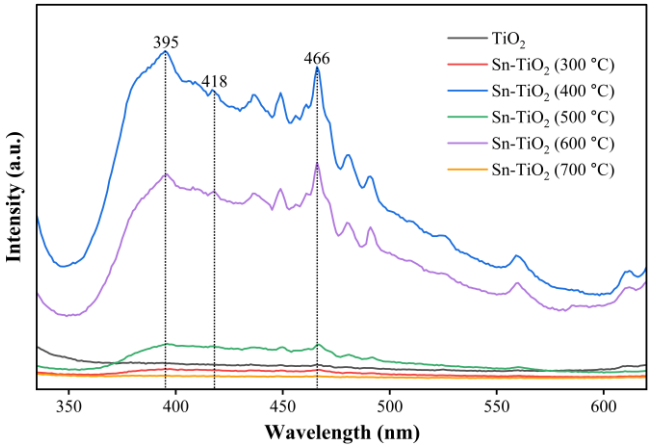

Figure 7. PL spectra of pure TiO_2 and Sn-doped TiO_2 photocatalysts

3.2 Photocatalytic degradation of MB

The photocatalytic performance of the prepared photocatalysts was evaluated by photodegrading MB under visible light irradiation. The degradation efficiency was determined by monitoring the decrease in MB absorbance throughout the irradiation period. For comparison, pure anatase TiO_2 was evaluated under identical experimental conditions to serve as a benchmark for the prepared Sn-doped photocatalysts. As illustrated in **Figure 8**, the degradation percentage of photocatalysts ranged from 46.2% to 65.2%.

Among the photocatalysts, Sn-TiO_2 (400 °C) exhibited the highest photocatalytic activity (65.2%). This superior performance was attributed to its narrowed band gap (3.14 eV) and high crystallinity. The reduced band gap facilitates enhanced visible-light absorption and generates a higher concentration of photo-induced charge carriers. Simultaneously, the high crystallinity reduces the density of structural defects that typically serve as recombination centres, thereby promoting efficient charge transport to surface active sites [54]. Furthermore, XRD analysis confirmed that this sample has a smaller crystallite size (66.78 nm) relative to pure TiO_2, which reduces the charge-carrier diffusion distance [55]. This optimal performance is consistent with previous studies indicating that 400 °C serves as a critical calcination threshold for maximizing photodegradation [56]. However, as a crystallite size of 66.78 nm is still inherently substantial, some degree of thermal grain growth and agglomeration likely occurs even at 400 °C, which partially restricts the overall photocatalytic efficiency.

In contrast, Sn-TiO_2 (600 °C) demonstrated the lowest efficiency (46.2%). This suppressed activity was primarily ascribed to thermal sintering, which caused particle agglomeration and grain growth, effectively reducing the available surface-active sites for MB adsorption and degradation. Additionally, its wider band gap (3.19 eV) restricted photon absorption and the subsequent generation of reactive oxygen species. Pure TiO_2 displayed moderate photocatalytic activity (61.0%), largely limited by its intrinsic wide band gap (3.24 eV), which restricts optical absorption to the UV region.

These results highlight that a calcination temperature of 400 °C is the optimal thermal threshold for balancing the structural and optical properties necessary for maximum degradation efficiency. Unexpectedly, pure TiO_2 exhibited higher photocatalytic performance compared to the Sn-TiO_2 (300 °C) and Sn-TiO_2 (600 °C) samples under visible light irradiation. This anomaly was likely due to incidental exposure to background UV radiation from ambient lighting during testing. Given that the anatase phase is highly responsive to UV excitation, pure TiO_2 effectively utilized this spectral fraction, thereby outperforming the aforementioned doped samples.

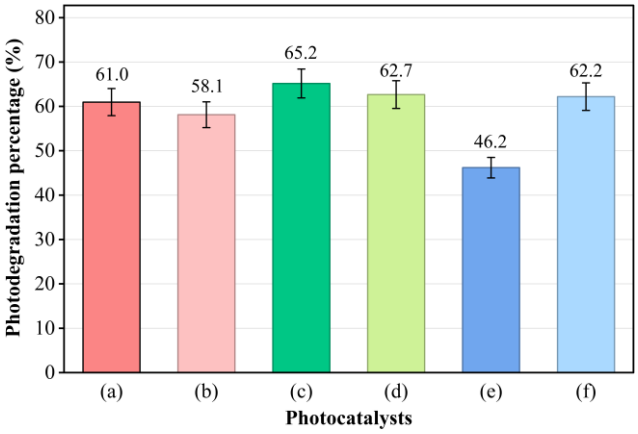

Figure 8. Photodegradation percentage of MB using (a) pure TiO_2, (b) Sn-TiO_2 (300 °C), (c) Sn-TiO_2 (400 °C), (d) Sn-TiO_2 (500 °C), (e) Sn-TiO_2 (600 °C), and (f) Sn-TiO_2 (700 °C). Error bars represent the variation between duplicate experimental runs ($n = 2$)

4. CONCLUSION

In this study, Sn-doped TiO_2 photocatalysts were successfully prepared via a hydrothermal method and calcined at different temperatures. While conventional literature predominantly focuses on optimizing dopant concentrations, this study isolates the effects of thermal processing by systematically varying the calcination temperature at a constant Sn loading to provide a clearer correlation between thermal conditions and the resulting physicochemical properties. The effect of calcination temperature on the physicochemical properties and photocatalytic performance of the photocatalysts was systematically evaluated through the photodegradation of MB. Characterization results confirmed that the samples crystallized exclusively in the anatase phase, with the successful incorporation of Sn into the TiO_2 lattice. Structural analysis further revealed that while Sn doping initially inhibited crystallite growth, increasing calcination temperatures promoted grain growth. DR UV-Vis analysis

confirmed that Sn doping effectively induced a red shift in the absorption edge, narrowing the band gap for the sample calcined at 400 °C. Among the tested photocatalysts, Sn-TiO_2 (400 °C) was the most efficient under visible light irradiation. This superior performance is driven by the relationship between its narrow band gap and high crystallinity, which together suppress non-radiative recombination and facilitate rapid charge carrier transport to surface-active sites. Overall, these findings demonstrate that an optimal calcination temperature of 400 °C is pivotal for balancing the structural and optical properties required to enhance the visible-light-driven performance of TiO_2-based photocatalysts for the effective treatment of dye-contaminated wastewater. This contributes valuable insights to the field of materials science by providing a deeper understanding of the processing-structure-property relationships under various processing conditions. Furthermore, by providing an efficient, visible-light-active treatment solution for persistent hazardous pollutants, this sustainable approach directly aligns with the United Nations Sustainable Development Goals, supporting Clean Water and Sanitation (SDG 6), Responsible Consumption and Production (SDG 12), and Life Below Water (SDG 14).

ACKNOWLEDGEMENTS

The authors would like to acknowledge the financial support obtained from the Ministry of Higher Education Malaysia (MOHE) and Universiti Teknologi Malaysia (UTM) through the Potential Academic Staff grant (Cost centre: QJ130000.2754.03K86).

REFERENCES

1. S. Benkhaya, S. M' rabet, A. El Harfi, Inorganic Chemistry Communications **115** (2020) 107891.
2. N. Parsafard, R. Abedi, H. Moodi, RSC Advances **14(28)** (2024) 19984-19995.
3. C. T. Hou, B. Hu, J. M. Zhu, Catalysts **8(12)** (2018).
4. P. Dey, P. Dey, M. B. Hoque, B. Baria, M. M. Rahman, S. Shovon, D. Das, Textile Research Journal **95(19-20)** (2025) 2472-2499.
5. R. B. Rajput, S. N. Jamble, R. B. Kale, Journal of Environmental Management **307** (2022) 17.
6. S. Ledakowicz, K. Paździor, Molecules **26(4)** (2021) 870.
7. A. Fujishima, K. Honda, Nature **238(5358)** (1972) 37-38.
8. A. S. M. Nur, M. Sultana, A. Mondal, S. Islam, F. N. Robel, A. Islam, M. S. A. Sumi, Journal of Water Process Engineering **47** (2022) 17.
9. R. K. Paul, M. Ahmaruzzaman, RSC Advances **15(38)** (2025) 31313-31359.
10. P. Kumari, A. Kumar, Results in Surfaces and Interfaces **11** (2023) 100122.
11. L. Predoana, E. M. Ciobanu, G. Petcu, S. Preda, J. Pandele-Cusu, E. M. Anghel, S. V. Petrescu, D. C. Culita, A. Baran, V. A. Surdu, B. S. Vasile, A. C. Ianculescu, Catalysts **13(3)** (2023).
12. S. Lee, A. Y. Cho, Y. S. Rim, J.-Y. Park, T. Choi, Coatings **10(6)** (2020) 557.
13. D. R. Eddy, M. D. Permana, L. K. Sakti, G. A. N. Sheha, Solihudin, S. Hidayat, T. Takei, N. Kumada, I. Rahayu, Nanomaterials **13(4)** (2023) 704.
14. A. Mukherjee, N. Bag, A. Chatterjee, J. Roy, S. Das, B. Chattopadhyay, A. Dey, Cleaner Water **4** (2025) 100105.
15. Y. Wei, Q. Wu, H. Meng, Y. Zhang, C. Cao, RSC Advances **13(30)** (2023) 20584-20597.
16. S. Mehraz, P. Kongsong, A. Taleb, N. Dokhane, L. Sikong, Solar Energy Materials and Solar Cells **189** (2019) 254-262.
17. A. Soleimani-Gorgani, H. E. Al-Hazmi, A. Esmaeili, S. Habibzadeh, Environmental Research **237** (2023) 9.
18. T. N. Trung, N. T. T. Kieu, D. Q. Ho, D. B. Seo, E. T. Kim, Journal of Materials Science **58(5)** (2023) 2156-2169.
19. X. Zhu, S. Han, W. Feng, Q. Kong, Z. Dong, C. Wang, J. Lei, Q. Yi, RSC Advances **8(26)** (2018) 14249-14257.
20. J. Li, J. Shi, Y. Li, Z. Ding, J. Huang, Ceramics International **47(6)** (2021) 8218-8227.
21. J. U. Rehman, S. Javed, M. Mujahid, O. Gohar, A. Ahmad, S. Brahma, M. B. Hanif, M. Motola, Physica B: Condensed Matter **690** (2024) 416260.
22. K. Santhi, S. Harish, M. Navaneethan, S. Ponnusamy, Journal of Materials Science: Materials in Electronics **33(12)** (2022) 9066-9084.
23. X. Zhu, S. Han, W. Feng, Q. Kong, Z. Dong, C. Wang, J. Lei, Q. Yi, RSC Advances **8(26)** (2018) 14249-14257.
24. R. Chandoliya, S. Sharma, V. Sharma, R. Joshi, I. Sivanesan, Plants **13(21)** (2024) 2964.
25. N. Kiraz, E. Burunkaya, Ö. Kesmez, H. E. Çamurlu, M. Asiltürk, Z. Yesil, E. Arpaç, Journal of Sol-Gel Science and Technology **59(2)** (2011) 381-386.
26. S. Phromma, T. Wutikhun, P. Kasamechonchung, T. Eksangsri, C. Sapcharoenkun, Applied Sciences **10(3)** (2020) 993.
27. N. Alduhisan, A. Al-Zahrani, Y. Al-Zahrani, H. Alghamdi, H. Kochkar, G. Berhault, B. Alqahtani, M. Alnasser, G. Alonizan, A. M. Ajeebi, M. Younas, Surfaces and Interfaces **78** (2025) 108097.
28. K. Maver, I. Arčon, M. Fanetti, S. Emin, M. Valant, U. L. Štangar, Catalysis Today **361** (2021) 124-129.
29. I. Rangel-Vázquez, G. Del Angel, V. Bertin, F. González, A. Vázquez-Zavala, A. Arrieta, J. M. Padilla, A. Barrera, E. Ramos-Ramirez, Journal of Alloys and Compounds, **643** (2015) S144-S149.
30. H. Hamdan, M. N. Mohd Muhid, S. L. Lee, Y. Y. Tan, International Journal of Chemical Reactor Engineering **7** (2009).
31. P. Pascariu, C. Cojocaru, M. Homocianu, P. Samoila, C. Romanitan, D. Nikolay, Ceramics International **49(7)** (2023) 10384-10394.
32. H. Thi Ngoc Suong, HUIT Journal of Science **25** (2025) 320-328.
33. R. D. Desiati, M. Taspika, E. Sugiarti, Materials Research Express **6(9)** (2019) 095059.
34. M. H. Razali, N. J. Roslan, U. M. Osman, M. Z. H. Rozaini, M. Yusoff, Malaysian Journal of Chemistry **22(2)** (2020) 37-42.
35. S. L. Lee, S. C. Wei, H. Nur, H. Hamdan, International Journal of Chemical Reactor Engineering **8(1)** (2010).
36. S. Arivazhaga, International Journal of Advance Research, Ideas and Innovations in Technology **4(2)** (2018) 2857-2860.
37. Y. Singh, H. Patel, A. Rai, S. Singh, N. Srivastav, P. Srivastava, Next Materials **8** (2025) 100680.
38. Y. K. Ooi, L. Yuliati, S. L. Lee, Chinese Journal of Catalysis **37(11)** (2016) 1871-1881.
39. H. Rasouli, F. Jafarpisheh, M. Ghorbanpour, Journal of Water and Environmental Nanotechnology **7(4)** (2022) 344-350.
40. R. Rajeswari, D. Venugopal, A. George, A. D. Raj, S. J. Sundaram, A. K. H. Bashir, M. Maaza, K. Kaviyarasu, Applied Physics A **127(7)** (2021) 498.
41. X. D. Zhu, L. X. Pei, R. R. Zhu, Y. Jiao, R. Y. Tang, W. Feng, Scientific Reports **8** (2018).
42. M. Alijani, B. K. Kaleji, Optical and Quantum Electronics **49(1)** (2017).
43. Y. Aristanti, Y. I. Supriyatna, N. P. Masduki, S. Soepriyanto, IOP Conference Series: Materials Science and Engineering **478(1)** (2019) 012019.
44. K. Ancy, C. Vijilvani, M. R. Bindhu, S. J. S. Bai, K. S. Almaary, T. M. Dawoud, A. Mubarak, M. S. Alfadul, Chemosphere **277** (2021) 130247.

45. G. Žerjav, K. Žižek, J. Zavašnik, A. Pintar, Journal of Environmental Chemical Engineering **10(3)** (2022) 107722.
46. M. A. Mohamed, W. N. Wan Salleh, J. Jaafar, M. S. Rosmi, Z. A. Mohd. Hir, M. Abd Mutalib, A. F. Ismail, M. Tanemura, Applied Surface Science **393** (2017) 46-59.
47. R.-C. Suciu, M. Zagrai, A. Popa, D. Toloman, C. Berghian-Grosan, C. Tudoran, M. Stefan, Inorganics **11(6)** (2023) 249.
48. N. I. A. Ghani, N. I. N. Zanal, N. S. M. Natar, S. R. Hamzah, M. A. Rosli, N. A. Muhamad, M. S. M. Azami, S. Mohamad, W. I. N. W. Ismail, Malaysian Journal of Chemistry **26(2)** (2024) 12-26.
49. S. B. Wategaonkar, V. G. Parale, S. S. Mali, C.-K. Hong, R. P. Pawar, P. S. Maldar, A. V. Moholkar, H.-H. Park, B. M. Sargar, R. K. Mane, Materials **14(21)** (2021) 6282.
50. Y. Guan, W. Liu, S. Zuo, K. Yuan, F. Wu, J. Ji, C. Yao, Journal of Materials Science: Materials in Electronics **31(24)** (2020) 22297-22311.
51. B. Koozegar Kaleji, M. Gorgani, International Journal of Environmental Analytical Chemistry **102(14)** (2022) 3357-3372.
52. Q. Qin, J. Wang, Y. Xia, D. Yang, Q. Zhou, X. Zhu, W. Feng, Catalysts **11(11)** (2021) 1341.
53. H. H. Nazari, L. Dejam, Physica B: Condensed Matter **626** (2022) 413461.
54. X. Zhu, J. Luo, Z. Dong, Z. Li, Y. Wu, Z. Cheng, X. Cao, Y. Wang, Y. Liu, Z. Zhang, Separation and Purification Technology **324** (2023) 124235.
55. S. N. Supardan, N. S. Sa'ari, S. A. Kamil, H. A. Rafaie, A. F. M. Fadzil, R. Fauzi, M. R. Mahmood, N. H. M. Noor, Journal of Physics: Conference Series **2680(1)** (2024) 012045.
56. X. Zhou, J. Lu, L. Li, Z. Wang, Journal of Nanomaterials **2011** (2011) 432947.